1
2
3
4
5
6
7
8
9
10
11
12
13
14
15
16
17
18
19
20
21
22
23
24
25
26
27
28
29
30
31
32
33
34
35
36
37
38
39
40
41
42
43
44
45
46
47
48
49
50
51
52
53
54
55
56
57
58
59
60
61
62
63
64
65

Concentration polarization model of spiral-wound membrane modules with application to batch-mode RO desalination of brackish water

T. Y. Qiu, P. A. Davies*

Sustainable Environment Research Group, School of Engineering and Applied Science, Aston University, Birmingham, B4 7ET, UK

* Corresponding author: E-mail: p.a.davies@aston.ac.uk,

Tel +44 (0)121 204 3724, Fax +44 (0)121 204 3683

1

ABSTRACT

Batch-mode RO (batch-RO) operation is considered a promising desalination method due to its low energy requirement compared to other RO system arrangements. To improve and predict batch-RO performance, studies on concentration polarization (CP) are carried out. The Kimura-Sourirajan mass-transfer model is applied and validated by experimentation with two different spiral-wound RO elements. Explicit analytical Sherwood correlations are derived based on experimental results. For batch-RO operation, a new genetic algorithm method is developed to estimate the Sherwood correlation parameters, taking into account the effects of variation in operating parameters. Analytical procedures are presented, then the mass transfer coefficient models are developed for different operation processes, i.e. batch RO and continuous RO. The CP related energy loss in batch-RO operation is quantified based on the resulting relationship between feed flow rates and mass transfer coefficients. It is found that CP increases energy consumption in batch RO by about 25% compared to the ideal case in which CP is absent. For continuous RO process, the derived Sherwood correlation predicted CP accurately. In addition, we determined the optimum feed flow rate of our batch-RO system.

Key words: batch-mode reverse osmosis (batch-RO), solar, high recovery, concentration polarization (CP), spiral-wound membrane (SWM), mass transfer

2

Symbol	Units	Description
a		constant
b		constant
C_{avg}	$kg \cdot m^{-3}$	average salt concentration across the membrane
C_b	$kg \cdot m^{-3}$	bulk concentration
C_f	$kg \cdot m^{-3}$	feed and permeate solute concentrations
C_m	$kg \cdot m^{-3}$	salt concentration on membrane
C_p	$kg \cdot m^{-3}$	feed and permeate solute concentrations
C_{p_ave}	$kg \cdot m^{-3}$	average concentration of permeate
CPF		concentration polarization factor
D	$m^2 \cdot s^{-1}$	diffusion coefficient
d_h	m	hydraulic diameter
J_s	$kg \cdot m^{-2} \cdot s^{-1}$	solute flux
J_v	$m \cdot s^{-1}$	permeate flux
k	$m \cdot s^{-1}$	mass transfer coefficient
L	m	channel length
L_p	$m^3 \cdot m^{-2} \cdot s^{-1} \cdot Pa^{-1}$	intrinsic membrane permeability
$OsmP$	Pa	osmotic pressure
$P_{power\_initial}$	Pa	batch-RO initial feed power pressure
P_s	$m \cdot s^{-1}$	salt permeability coefficient
P_s'	$mol \cdot m^{-2} \cdot s^{-1} \cdot Pa^{-1}$	salt permeability coefficient
Q_f	$m^3 \cdot s^{-1}$	feed flow rate
Q_p	$m^3 \cdot s^{-1}$	permeate flow rate
R		real rejection fraction
Re		Reynolds number
R_o		observed membrane rejection fraction

Sc		Schmidt number
SEC	kWh·m^{-3}	specific energy consumption
Sh		Sherwood number
u	m·s^{-1}	crossflow velocity
v	m^2·s^{-1}	kinematic viscosity
α		constant
β		constant
γ		constant
δ	m	layer of thickness
$\Delta OsmP$	Pa	difference in the osmotic pressure across the membrane
ΔP	Pa	operating pressure
σ_1		reflection coefficient
σ_2		coefficient of coupling between salt and water

Abbreviations

BW	Brackish water
CP	Concentration polarization
KS	Kimura-Sourirajan
PV	Photovoltaic
RES	Renewable energy source
RO	Reverse osmosis
SWM	Spiral-wound membrane

4

1. Introduction

Reverse osmosis (RO) membrane desalination driven by renewable energy (RE) sources has been identified as an effective method to address two of the most pervasive global problems: the energy crisis and water shortage [1]. Among all the RE-powered desalination technologies, solar-driven RO has been gaining popularity in the last decades [2] due, in part, to the low energy requirement of RO relative to other technologies and the abundant solar energy in arid and semi-arid areas. A number of solar photovoltaic reverse osmosis (PVRO) seawater desalination systems have been implemented throughout the world, especially in the middle east and north Africa (MENA) region, with an overall capacity of around 300 m^3/day [2]. A number of brackish water PV-RO systems have also been reported [3]. The energy efficiency ratio (which compares performance to the thermodynamically ideal case) for the brackish water (BW) systems is lower than for seawater solar PV-RO systems – indicating greater scope for improvement [4]. Solar PV-RO BW systems can solve the lack of access to electricity and fresh water in remote inland areas, but the major drawbacks holding back the application of such systems are their low efficiencies and low recovery ratios.

For the application of solar-powered BWRO systems in remote, semi-arid areas, PV is not necessarily the best choice of energy source. This is not only because of the high price and maintenance cost of solar cells, but also their low efficiency. The relatively small components of PV-RO systems, e.g. inverter and pumps, lower the system performance further. Besides the low efficiency, the recovery ratio of a solar PV-RO BW system is typically low, meaning that a small fraction of fresh water is produced, with a large volume of reject brine. Brine disposal is frequently a problem, especially when it comes to inland desalination systems, because direct brine discharge can cause environmental pollution and brine treatment methods require additional technical and financial support [5]. These critical drawbacks of current solar PV-RO BW systems have led to a search for alternative energy sources and inland desalination technologies. For example, Papadakis and co-workers at the University of Athens developed an organic Rankine cycle RO system for both sea and brackish water [6, 7]; and a Rankine cycle batch-mode RO (batch-RO) method was proposed by Davies [8]. Batch-RO uses mechanical energy generated

5

from vapour expansion to provide the operation pressure for the RO separation process. Results have shown that batch-RO is able to achieve a high efficiency as well as a high recovery ratio [9]. Additionally, besides solar energy, other heat sources such as waste heat and biomass energy are also applicable to batch-RO especially when used in co-generation systems.

Through pilot experiments to develop the batch-RO system, two major energy loss mechanisms — dispersion and concentration polarization (CP) — have been identified and investigated to improve system performance. The study of dispersion has been published in earlier paper by the authors [10]. In this paper, CP investigated in detail.

In membrane separation, water penetrates the membrane from the feed side towards the permeate side, when the applied pressure overcomes the osmotic pressure difference. Rejected salts accumulate on the membrane surface and build up a layer of high concentration; this phenomenon is referred to as concentration polarization. CP significantly worsens the performance of membrane separation processes since the osmotic pressure difference depends on the concentration difference across the membrane, which is the major factor in determining the operating pressure. Hence, understanding mass transfer and controlling CP are essential in improving the performance of RO separation. Such qualitative and quantitative understanding can be gained by determining the mass transfer coefficient and membrane transport parameters based on various transport models [11, 12]. Among these solute transport characteristics models, the film model, and its two variants with either a mechanistic approach (Kimura-Sourirajan model) or a thermodynamic approach (Spiegler-Kedem model) have been most widely used, as they do not require detailed information on the structure of the RO membrane, which cannot readily be described by simple quantitative parameters [13]. These models have been carefully examined in several studies presented in the literature to characterise the solute transport in nanofiltration membranes [13-17], ultrafiltration membranes [18, 19], and RO membrane of simple structures, i.e. tubular or flat cell, [20-22]. The conclusion about the mechanism of solute separation by membranes is still a matter of controversy and indeed this mechanism may vary according to the type of specific RO membranes.

6

In contrast to the plethora of CP research on conventional (continuous steady mode) RO process, no studies pertaining to CP in batch-RO have been carried out, because not many commercially available batch-RO systems exist and research on batch-RO is at a relatively early stage [23-25]. Therefore, research about CP in batch-RO is necessary to obtain insight into the characteristics of mass transfer in transient hydrodynamic conditions as well as to contribute to the improvement of batch-RO. Additionally, although previous studies provide informative insights into CP phenomena in RO modules with simple structures, they cannot currently be considered representative or accurate for CP in the specific spiral-wound membrane (SWM) RO elements used in this study.

The objectives of this paper are to elucidate the mass transfer characteristics of different SWM RO elements and to investigate systematically mass transfer coefficients as well as CP using semi-experimental methods, thus providing guidance on the optimal design of the batch-RO system. To quantitatively assess CP values, we derived corresponding Sherwood correlations to reveal the relationship between flow rate and the mass transfer coefficient. In addition, we also quantified the CP-related energy loss in the batch-RO system.

2. Theories

2.1 Film model

The film model assumes a one-dimensional flow and a fully developed CP layer. At steady state, as shown in *Figure 1*, the solute flux, passing through the membrane J_s (kg·m^{-2}·s^{-1}) is balanced by the convective flux $J_v·C$ and the solute diffusive flux from the membrane wall to the bulk solution $D·dC/dx$,

$$J_s = C_p \cdot J_v = J_v \cdot C \quad - D \cdot \frac{dC}{dx} \tag{1}$$

where C and C_p are the feed and permeate solute concentrations (kg·m^{-3}), respectively, J_v is the permeate flux (m·s^{-1}), and D is the diffusion coefficient (m^2·s^{-1}).

The solution of *Eq. (1)* for a boundary layer of thickness δ (m) gives:

$$CPF = \frac{C_m - C_p}{C_b - C_p} = exp\left(\frac{J_v}{k}\right) \tag{2}$$

Where CPF is the concentration polarization factor, C_m and C_b (equals the feed concentration) are the solute concentrations (kg·m^{-3}) at the membrane surface and in the bulk solution, respectively. k is the mass transfer coefficient (m·s^{-1}) and is defined as:

$$k = \frac{D}{\delta} \tag{3}$$

Eq. (2) indicates that *CPF* is strongly dependant on the permeate flux J_v and mass transport coefficient k.

The observed membrane rejection fraction R_o is given by:

$$R_o = \frac{C_b - C_p}{C_b} \tag{4}$$

And the real rejection fraction R is given by:

$$R = \frac{C_m - C_p}{C_m} \tag{5}$$

Writing *Eq. (2)* in terms of observed rejection fraction R_o and real rejection fraction R gives:

$$\frac{1 - R_o}{R_o} = \frac{1 - R}{R} \cdot exp\left(\frac{J_v}{k}\right) \tag{6}$$

Rearranging *Eq. (6)* arrives at:

$$ln\left(\frac{1 - R_o}{R_o}\right) = \frac{J_v}{k} + ln\left(\frac{1 - R}{R}\right) \tag{7}$$

2.2 KS model

The Kimura-Sourirajan (KS) model, also known as the combined solution-diffusion/film model, assumes that the solvent and solute fluxes do not interact with each other [26] and the solute is transported solely by diffusion [17].

In the KS model, the solvent flux J_v through the membrane is given by:

$$J_v = L_p \cdot (\Delta P - \Delta OsmP) \tag{8}$$

The solute flux J_s according to KS model is expressed as:

$$J_s = P_s \cdot (C_m - C_p) \tag{9}$$

where L_p is the intrinsic membrane permeability ($m^3 \cdot m^{-2} \cdot s^{-1} \cdot Pa^{-1}$), i.e., pure water permeability, ΔP is the operating pressure (Pa), and $\Delta OsmP$ is the difference in the osmotic pressure across the membrane (Pa), which equals to $(OsmP_m - OsmP_p)$. P_s is the salt permeability coefficient ($m \cdot s^{-1}$), which characterizes solute transport through the membrane.

Combining *Eqs. (5)*, *(6)* and *(9)* to eliminate the unknown parameters C_m and R gives:

$$\frac{J_v}{k} = ln\left(\frac{1 - R_o}{R_o}\right) - ln\left(\frac{P_s}{J_v}\right) \tag{10}$$

2.3. Sherwood correlation

Most of the mass transfer models adopted in the characterization of RO or ultrafiltration membranes make use of the Sherwood correlation [11, 17, 27]. The Sherwood correlation indicates the extent to which mass transfer rate is affected by Reynolds number, i.e., flow regime, and hydraulic conditions.

For fully developed turbulent and laminar flows, the generalized correlations of mass transfer coefficient k have the following empirical forms, respectively [27-30]:

$$Sh = \frac{k \cdot d_h}{D} = a \cdot Re^\alpha \cdot Sc^\beta = a \cdot \left(\frac{u \cdot d_h}{v}\right)^\alpha \cdot \left(\frac{v}{D}\right)^\beta \tag{11}$$

$$Sh = \frac{k \cdot d_h}{D} = a \cdot Re^\alpha \cdot Sc^\beta \cdot \left(\frac{d_h}{L}\right)^\gamma$$
$$= a \cdot \left(\frac{u \cdot d_h}{v}\right)^\alpha \cdot \left(\frac{v}{D}\right)^\beta \cdot \left(\frac{d_h}{L}\right)^\gamma \tag{12}$$

where a, α, β and γ are constants that vary for different diffusion physical situations, and they can be determined experimentally. Sh is the Sherwood number, Re is the Reynolds number, Sc is the Schmidt number, u is the crossflow velocity ($m \cdot s^{-1}$), v is the kinematic viscosity ($m^2 \cdot s^{-1}$), L is the channel length (m) and d_h is the hydraulic diameter (m).

The Sherwood correlations, i.e. *Eqs. (11)* and *(12)*, indicate that the Sherwood number varies with Reynolds number and Schmidt number, the Schmidt number being a characteristic of diffusion. In other words, the mass transfer coefficient k is in essence a function of the crossflow velocity u, diffusion coefficient D, fluid properties, and the membrane module configurations.

Most of the mass transport models for membrane separation use some specifically tuned Sherwood correlation to quantify the concentration at the membrane wall C_m. For a fully developed turbulent flow, one widely used Sherwood correlation is [27]:

$$Sh = 0.023 \cdot Re^{0.8} \cdot Sc^{0.33} \qquad (13)$$

For a fully developed laminar flow, it has the form [28]:

$$Sh = 1.86 \cdot \left(Re \cdot Sc \cdot \frac{d_h}{L} \right)^{1/3} \qquad (14)$$

For practical SWM RO elements, the spiral geometry can be adequately approximated by an unwound flat rectangular membrane channel. Because the feed channel is too narrow and the mean crossflow velocity is usually less than 0.8 $m \cdot s^{-1}$, turbulent flow is unlikely to be fully developed, and laminar flow may sometimes be assumed. However, the occurrence of re-circulation regions, resulting from the increased local shear rates and velocities due to the feed channel spacers [31], suggests that flow is not purely laminar but is undergoing transition. Thus, most existing Sherwood correlations reported in the literature for fully developed turbulent or laminar flow may not be suitable for the determination of mass transfer coefficient in the RO SWM elements used in this study.

3. Experimental approach

For a batch-RO system, the operating parameters vary during the process; conversely, the parameters are usually constant in continuous RO systems. Thus, different methodologies are applied to the determination of mass transfer coefficient k in these two modes of operation. After the mass transfer coefficients are determined, the specific Sherwood correlations are estimated.

3.1. Batch mode operation

For the batch-RO operation, a graphical method is adopted here. From *Eq. (12)*, the relationship between the feed velocity u and mass transfer coefficient k is of the form:

$$k = \frac{u^{\alpha}}{b} \tag{15}$$

Substituting *Eq. (15)* in *(10)* and re-arranging with substitution from *Eq. (4)* gives:

$$ln\left(J_v \cdot \frac{C_p}{C_b - C_p}\right) = ln\, P_s + b \cdot \frac{J_v}{u^{\alpha}} \tag{16}$$

Eq. (16) provides a linear relationship between $ln\left(J_v \cdot C_p/C_b - C_p\right)$ and J_v/u^{α}. On the basis of experimental results for the batch-RO, which are measured at various flow velocities and various feed pressures, the value of the velocity exponent α is determined from the best linear fit of the measurements from which both the salt permeation parameter P_s and the coefficient b can be obtained. The Sherwood relationship can then be easily worked out with the known parameters α and b based on *Eq. (12)*.

3.2. Continuous operation

In conventional continuous operation, because of the constant feed concentration, a straight forward experimental procedure was used [22]:

For pure water, based on *Eq. (8)*:

$$(J_v)_{water} = L_p \cdot \Delta P \tag{17}$$

Thus, using a linear parameter estimation method, with the data for J_v obtained at different operating pressures while maintaining a constant feed flow rate for each experiment with pure water, the intrinsic membrane permeability L_p was estimated. Then, a series of experiments was performed for different feed flow rates with a constant feed concentration and operating pressure. With measured permeate flux J_v and permeate concentration C_p (used to calculate $OsmP_p$) the concentration at the membrane surface π_m (calculated from $OsmP_m$) was calculated based on *Eq. (8)*. The values of CPF and mass transfer coefficient k were subsequently obtained using *Eq. (2)*. The Sherwood relationship can then be easily worked out with the known mass transfer coefficient k based on *Eq. (12)*.

4. Experimental set-up and procedure

Each experiment used a single module and RO membrane element of commercial polyamide thin-film-composite type, either BW30-2540 (brackish water membrane) or XLE-2540 (low energy membrane) type. Both were from Dow® FilmTec® and in the spiral wound element form. Given the diameter of the element and the total membrane area provided by the manufacturer, the feed flow channel height and width were determined accordingly. The two membrane elements were of the same size, i.e. 0.06 m in diameter and 1 m in length. The average flow channel height was 7.1×10^{-4} m, with the channel length and width being 1 and 1.3 m, respectively. Both of the elements have 2.6 m^2 active membrane area, but with different salt rejection ratios being 99.5% for BW membrane and 99% for XLE membrane. According to the data provided by the manufacturer, the pure water permeabilities of the two membrane elements are: 9.14×10^{-12} m·s^{-1}·Pa^{-1} for the BW membrane element and 2.03×10^{-11} m·s^{-1}·Pa^{-1} for the XLE membrane element.

4.1. Batch mode operation

The batch-RO set up (*Figure 2*) has been described in an earlier paper [9]. The paper introduced a batch-RO system powered by compressed air, referred to as DesaLink, which (*Figure 3*) was also used to conduct experiments in the current study. Different re-circulating flow rates were tested to reveal the relationship between mass transfer characteristics and unstable hydraulic

12

conditions. For all the experiments, the feed concentrations and feed air pressures were kept constant at 2.5 kg·m^{-3} (2500 ppm) and 8×10^5 Pa (8 bar), respectively. The average feed flow rates were 0.04, 0.03 and 0.026 $\times10^{-3}$ m^3·s^{-1} (2.4, 2.0 and 1.6 l·min^{-1}) in separate runs. Experiments were conducted three times to reduce random errors.

4.2. Continuous operation

A schematic diagram of the experimental unit is illustrated in *Figure 4*. The unit consists of a single membrane element, feed pump, water reservoir and pulsation dampener. The pulsation dampener from manufacture *Reflex N* was installed between the feed pump and the membrane element to smooth the feed flow from the pump. The *Wilo* re-circulation pump was installed before the membrane element. Concentrate and permeate flows were mixed in a bucket prior to filling the feed tank. Feed solution was prepared using desalinated tap water with an electrical conductivity less than 0.1 μS·cm^{-1} and analytical grade sodium chloride (NaCl) salt from Fisher Scientific. The operation pressure and feed flow rate were simultaneously controlled by adjusting the power supply and the throttle valve located at the brine outlet. Both concentration and temperature of the permeate flux were monitored by a *EUTECH COND 500* conductivity transmitter which included a temperature-measuring function. The conductivity of the feed solution in the water tank was measured using a *Hanna HI 8733* conductivity meter. The concentrations of solution were calculated from the conductivity measurements using specific conductance for NaCl at specific temperatures. Both the concentrate and permeate flow rates were measured with a stop watch and measuring cylinders. The concentration of concentrate flow was calculated based on the conservation of mass.

Prior to the experiments, two brand new membrane elements, named BW30-2540 and XLE-2540, were conditioned by feeding 3 kg·m^{-3} (3000 ppm) NaCl solution for 12 hours at 9×10^5 Pa (9 bar), in order to wet the RO membrane completely. The mass transport experiments were carried out with 800 ppm NaCl solution at the fixed operation pressure of 2.76×10^5 Pa (2.76 bar). The feed flow rates were varied by adjusting the supply pump power. In all cases, the membrane processes were stabilized for 1 hour before taking the measurements, carefully ensuring the

13

permeate concentration and flow rate had stabilised, i.e. the system had reached a steady state. The bulk solution coming out of the membrane element and the permeate were sampled simultaneously. All the experiments were performed in the temperature range of 298.15±0.5 K (23±0.5 °C).

5. Results and discussion

5.1. Salt transport characteristics

For continuous RO operation, the salt transport characteristics in different membrane elements were illustrated in *Figure 5*, and elucidated by the variation of observed salt rejection fraction R_o (calculated using *Eq. 4*) with permeate flux J_v. For both membrane elements, the observed salt rejection fraction R_o is slightly lower for the feed solution of a higher concentration. For the BW membrane element only around 1% difference in R_o was observed for all the concentrations of feed solution ranging from 0.06 kg·m^{-3} (60 ppm) to 5 kg·m^{-3} (5000 ppm), while approximately 2% difference in R_o was observed for the XLE membrane element in the same concentration range. It thus can be argued that the salt rejection property of membranes is trivially affected by the concentration of feed solutions, at least for the range of interest in our work. Both of the elements displayed high salt rejection fractions; the average values of R_o for the BW and XLE membrane elements were 95% and 90%, respectively. For the XLE element (*Figure 5a*), the R_o was less than 60% at low J_v (approximately 1.0×10^{-6} m·s^{-1}), but it rapidly increased and reached almost 90% when J_v was 2.3×10^{-6} m·s^{-1}. The R_o of XLE element dropped off beyond the value of 6.9×10^{-6} m·s^{-1}, in contrast, for the BW membrane element (*Figure 5b*), R_o remained almost constant with increasing solvent flux J_v. As the permeate flux increased to about 2.3×10^{-6} m·s^{-1} permeate flux and above, the R_o reached about 92% and levelled off thereafter.

Based on the film model, *Eq. (7)*, it is noted that when the true salt rejection R is independent of permeate flux J_v, the observed solute removal R_o is determined by J_v directly; this is supported by the results shown in *Figure 5*. According to *Eq. (1)*, if the solute passing through the membrane J_s increases (means accordingly decreased observed solute removal fraction R_o) with increasing solvent flux J_v, then it can be established that the solute transport through the

14

membrane is dominated by convection (convective flux $J_v \cdot C_f$). The salt transport characteristic of the XLE element (*Figure 5)* is in line with this description, i.e., R_o decreases at high solvent flux J_v. On the other hand, when the solute transport is dominated by diffusion, R_o monotonically increases until it levels off with increasing J_v, which is demonstrated by the BW element results (*Figure 5)*.

Beside the experimental results of the steady operation (continuous RO) that demonstrate the different mass transfer mechanisms in different RO elements, the experimental results (*Figure 6)* of the un-steady operation (batch mode) have also indicated a similar trend. For the XLE membrane (*Figure 6a*), the average concentration of the permeate C_{p_ave} is increased (decreased R_o) with increasing operation pressure (increasing J_v). For the BW membrane *(Figure 6b)*, the reversed trends are observed, the C_{p_ave} is decreased (increased R_o) with increasing operating pressure (increasing J_v). Notably, for feed water of 4 kg·m^{-3} (4000 ppm) solute, the product permeate in conjunction with the XLE element had an average concentration above 0.5 kg·m^{-3} (500 ppm, drinking water limit); thus the XLE element was not used in batch-RO operation.

The results above show that for continuous (steady) and batch-RO (transient) processes, the KS model, which suggests the solute is transported solely by diffusion, describes well the mass transfer characteristic in BW element. Though this model described less well the results for the XLE module in general, for high rejection ratios such as encountered in practice it gives an adequate description. For comparison, the relative contributions of the diffusive and convective fluxes in the Spiegler-Kedem model [32] are mainly dependent on the hydraulic conditions, such as feed concentration, feed flow rate and operation pressure. In practical batch RO applications, the concentration of feed solution is in the range of 3–10 kg·m^{-3} (3000–10000 ppm) during the pressurisation cycle, and the average permeate flux J_v is in the range of 2.3×10^{-6}–4.6 ×10^{-6} m·s^{-1} accordingly, from *Figure 5(a)*, it is seen that the observed salt rejection R_o within this J_v range is above 90% and remains almost constant, indicating the salt transport due to convective flux is very small and what follows is its diffusion-only characteristic. Additionally, small deviations in R_o caused by the different feed concentrations can be neglected. This simplification is supported by the work of Ghiu [17], who found that the KS and is similar to the Spiegler-Kedem model when the solute

15

rejection ratio R_o was higher than 86%. Taking into account this argument as well as our experimental results, the combined film/KS model was considered as having minimal deficiencies and was therefore applied to describe the transport mechanism and determine the mass transfer coefficient k for both XLE and BW membrane elements.

5.2. Mass transfer in batch-RO process

The feed flow rate varies during the batch-RO operation; thus, the experimental data from one pressurization process (*Figure 2*) reveal the relationship between the different feed flow and mass transfer coefficients. However, in order to derive the relationship between the average feed and permeate flows (which was used in the modelling process in authors' another study), different initial feed flow rates were used in the tests (*Figure 7*).

The obtained permeate flows Q_p for the corresponding different feed flow rates Q_f are shown in *Figure 8*. Note that only the large and small feed flow rates are presented in *Figure 8,* due to the small differences between the medium and small feed flow rates. As expected, the permeate flow rate was directly affected by the feed flow rate. Furthermore, not only were the observed permeate flows different, but the total salt passages also varied under the varying feed flow conditions (*Figure 9)*. For the batch system, pressure, feed flow and concentration all vary with time, which explains the more complicated pattern of results than normally seen in a continuous flow system.

Both *Figures 8* and *9* point to the fact that the permeate quality is dependent on the average feed flow rate. When the average permeate flow rate is higher (meaning a larger volume of permeate) the salt passage is reduced (meaning a lower concentration of permeate). This is because large flow rates enhance the mass transfer and therefore reduce the CP. It thus emphasizes the need to construct a specific theoretical model which describes the relationship between flow rates and mass transfer coefficients for unsteady batch-RO operation. This would, in turn, allow for the quantification of the observed proportional change in permeate qualities, i.e. volume and concentration, against various average feed flow rates.

16

A genetic algorithm (GA) (available in *Matlab*® toolbox) was used to fit *Eq. (16)* to the batch-RO process. In brief, genetic algorithms, as distinct from most classical, derivative-based optimization strategies, are heuristic search techniques inspired from the biological process of evolution by means of natural selection. GAs are efficient for function minimization in a complex search landscape with possibly strongly correlated adjustable parameters [33]. For the objective functions, ordinary least-squares (OLS) estimation was first used to fit the data. Moreover, to guarantee the goodness of fit and diminish possible chance correlations between the fitted parameters, another approach, termed robust regression (RR), was also employed. This is because OLS can behave badly when the error distribution is not normal and the number of adjustable parameters is somewhat large relative to the number of data points to be modelled, whereas, RR is less vulnerable to unusual data points and can normally circumvent such problems. All fittings using either OLS or RR plausibly arrived at almost identical sets of parameters, which display a clear indication of the fitness of the resulting Sherwood correlations.

All the unknown parameters, namely α, β, γ and a (based on *Eqs. 11, 12 and 16*) were estimated simultaneously by the GA implementation, yielding a very satisfactory regression coefficient R^2 (*Figure 11*). The variables Sh, Re, Sc, d_h and L were obtained from the experiments. Then, the unknown coefficients (α, β, γ, a) were determined by fitting the experimental data to Eq. (11) using GA (for further details of this procedure see [34]).This led to the following Sherwood correlation:

$$Sh = \frac{k \cdot d_h}{D} = 2.09 \cdot Re^{0.26} \cdot Sc^{0.38} \cdot \left(\frac{d_h}{L}\right)^{0.33} \tag{18}$$

In the literature, a value of $\alpha = 1/3$ (*Eq.14*) is typically suggested for the exponent of Re for a fully developed laminar flow [28]. Nonetheless, based on the fit of *Eq. (18)* to the experimental data, it is concluded here that for a partially laminar (transition) flow in the SWM RO element, a new model (*Eq. 18* with α=0.26) rather than the empirical Sherwood correlation (*Eq. 14*) is needed to characterise correctly the system. So, the herein developed Sherwood correlation obtained by

17

the GA fitting was chosen as the more appropriate and accurate correlation for a transition flow in RO module, and the conventional value of α =1/3 was not used.

With known constants a, α, β and γ, the mass transfer coefficients k were then calculated based on *Eq. (18)*. The obtained mass transfer coefficients k were plotted against the corresponding feed flow velocities, demonstrating a clear increase of the mass transfer coefficients k with increasing feed flow velocity u (*Figure 12*).

With the mass transfer coefficients k determined, the *CPFs* were obtained based on *Eq. (2)*. The increasing CPF against time (*Figure 13*), was due to the increase of permeate flow rate and the decrease of feed flow rate along the time. At any given time point, the *CPF* was larger for the operation with the small feed flow rate, affirming again the large flow rates help to reduce the CP. This is also in line with the expectation from the Sherwood correlation (*Eq. 18*).

5.3. Mass transfer in continuous RO process

For steady continuous RO process, both of the BW and XLE SWM elements were tested. According to the procedure described in Section 4.2, the vales of *CPF* were calculated (*Figure 14*) using *Eqs. (17), (8)* and *(2)* subsequently. It shows the *CPF* value is reduced with a higher crossflow velocity u, which is in line with the theory. For the BW membrane, the *CPF* value is lowered by 25 % from 1.6 to 1.3 in the crossflow rate range of 1.8×10^{-2} –11.5×10^{-2} m·s^{-1}. For the XLE membrane element, similar trends of *CPF* values were found. The slightly larger *CPF* values compared to the BW system can be explained by the larger permeate flux obtained with the XLE membrane element.

Based on the obtained *CPF* values and *Eq. (2)*, the corresponding mass transfer coefficients k are calculated and summarized in *Figure 15*. It shows that, in the crossflow velocity range investigated, there is a significant enhancement in the mass transfer coefficient k with increasing crossflow velocity u. The decreased *CPF* values can be attributed to the increase of back-diffusive transport of the salt away from the membrane surface. For the XLE element, which was operated in the crossflow velocity range of 5×10^{-2} – 12×10^{-2} m·s^{-1}, this shows the mass transfer coefficients were increased by 40% (from 6.4×10^{-6} to 9×10^{-6} m·s^{-1}) (*Figure 15a*). The

18

mass transfer coefficients for the BW membrane element system were doubled (from 3.8×10^{-6} to 7.3×10^{-6} m·s^{-1}) in the crossflow velocity range of $2 \times 10^{-2} - 12 \times 10^{-2}$ m·s^{-1} (*Figure 15b*). In comparison to the BW membrane element system at the similar crossflow velocities, the slightly higher mass transfer coefficients for the XLE membrane element may be explained by minor differences in membrane and spacer geometry, which may be influenced by the different operating pressures in each case.

With the calculated Sherwood number *Sh*, Reynolds number *Re* and Schmidt number *Sc*, the relevant constants in *Eq. (12)*, namely a, α, β and γ, were determined by GA method. Thus, the specific Sherwood correlations for both of the studied BW and XLE elements were established. It needs to be noted that the feed flow channel of the two membrane elements were the same, in other words, the third term $(d_h/L)^\gamma$ in *Eq. (12)* was fixed. However, the channel geometry constraints were still included in the determination of the Sherwood correlations in order to generalize the correlation for other commercially available SWMs with different feed channel heights and lengths.

The experimentally determined relationship between the dimensionless numbers *Sh* and *Re* is shown in *Figure 6*. With the constants optimised following the procedure described above, the Sherwood correlations can be rewritten as follows:

for the BW30-2540 membrane element:

$$Sh_{BW} = 0.93 \cdot Re^{0.33} \cdot Sc^{0.34} \cdot \left(\frac{d_h}{L}\right)^{0.33} \tag{19}$$

for the XLE-2540 membrane element:

$$Sh_{XLE} = 1.1 \cdot Re^{0.34} \cdot Sc^{0.34} \cdot \left(\frac{d_h}{L}\right)^{0.33} \tag{20}$$

A satisfactory representation of the experimental data was provided by these two correlations. This is clearly observable from: (1) the good agreement between the experimental and predicted data in terms of both the shape of the curve and the overlap of data points (*Figure 16)* and (2) the regression coefficients (R^2) which are more than 0.99, as indication of the goodness of fit (*Figure 17)*.

Comparing *Eqs. (19)* and *(20)* for the BW and XLE membrane element system respectively, it should be noted that the constant (β) relating to the Schmidt numbers (*Sc*) and the constant (γ) relating to the channel geometry term (d_h/L) are the same in both equations. The *Re* related constants (α) are very similar. There is a noticeable difference in the constant a, suggesting that the difference between the two correlations is mainly due to the difference of the inlet zone of the membrane elements, as the hydrodynamic conditions used in all experiments (including the characteristics of feed solutions and channel geometries of each membrane element) were identical.

It needs to be emphasized that care must be taken when selecting the correlation models for specific RO systems. We find some of the commonly used correlations for fully developed laminar flows may not be used for the SWM RO elements investigated in this study. In contrast, our newly established Sherwood correlations showed semi-quantitative to quantitative agreement with the experiments over a wide range of crossflow velocities; thus, the accuracy and applicability of the Sherwood correlation were confirmed. It can be concluded that the Sherwood correlations established in this work for the BW30-2540 and XLE-2540 SWM elements can be used to determine the mass transfer coefficients for salt solutions in continuous operation processes with a satisfactory accuracy.

5.4. Related energy losses in DesaLink

The ideal specific energy consumption (SEC_{ideal}), i.e. with no CP related energy losses, of a batch-RO desalination process for BW is related to the osmotic pressure of the feed solution *OsmP* and the recovery ratio *r*:

$$SEC_{ideal} = \frac{OsmP}{r} \cdot ln\frac{1}{(1-r)} \qquad (21)$$

For a practical system, where CP is inevitable, the SEC increases proportionally to the CP factor (CPF) because the $OsmP$ increased in proportion to CPF. Furthermore, extra energy consumption occurs because of the use of the re-circulation pump. The amount of energy consumed by the re-circulation is related to the feed flow rate and operation time. Thus, the specific energy consumption SEC of the practical batch-RO desalination process is expressed as the sum of two terms:

$$SEC = CPF \cdot SEC_{ideal} + SEC_{pump} \qquad (22)$$

where SEC_{ideal} is the specific energy consumption without concentration polarization, and SEC_{pump} is the specific energy consumption of the re-circulation pump. The CPF can be quantified based on *Eq. (2)* and the newly established Sherwood correlation, *Eq. (19)*. SEC_{ideal} is calculated based on *Eq. (21)*. The energy consumption of the pump is assumed to increase linearly with the feed flow rate. With the known volume of permeate, which equals the volume of the pump cylinder (refer to Figure 3) and permeate flux, the SEC_{pump} is given as follows:

$$SEC_{pump} = \frac{f(u) \cdot t}{V_p} = \frac{f(u) \cdot \frac{V_{water}}{Q_p}}{V_{water}} = \frac{f(u)}{Q_p} \qquad (23)$$

where V_p is the volume of permeate water (L), which equals the volume of the water cylinder V_{water} (L), and t is the operation time (s), which equals the volume of water cylinder divided by the rate of permeate flow Q_p.

The parameters of Q_p and feed concentration C_f were selected according to the DesaLink operation range. In light of the batch-RO system test results, the values for Q_p and C_f were chosen to be 1×10^{-5} m$^3 \cdot$s^{-1} (0.6 l$\cdot$min^{-1}) and 8000 ppm, respectively. And the energy needed by the re-

circulation pump, which is a function of the feed flow rate, was decided according to the pump test results. In *Eq. (22)*, the first term, $CPF \cdot SEC_{ideal}$, decreases with the feed flow rate u exponentially. The second term, SEC_{pump}, increases with u linearly. Therefore, there exists an optimum point at which the minimum SEC is achieved. *Figure 17* thus illustrates the changes of the $CPF \cdot SEC_{ideal}$, SEC_{pump} and their sum respectively, and a value of 2 l min^{-1} for feed flow rate can be identified graphically to yield the optimum SEC. When the optimal re-circulation flow (i.e. 2 l min^{-1}) is applied, an average value of 1.25 was obtained for CP; this value suggests 25% energy loss due to CP. The fact that there exists an optimal re-circulation flow for our batch-RO system means that the lowest SEC is achieved when the ratio between re-circulation flow and produced permeate flow is 3. A larger re-circulation flow would result in energy inefficiency due to increased energy consumption by the re-circulation pump, while a smaller flow would lead to an increased CP layer which also decreases the overall system efficiency. Likewise, this optimal ratio between re-circulation flow and permeate flow can be applied in operation for similar systems with different size.

6. Conclusion

For inland applications, batch-RO desalination has shown advantages in BW desalination over conventional continuous BWRO because of the high recovery ratio achievable without high energy input. Moreover, batch RO allows greater control over CP through adjustment of the re-circulation flow rate. Thorough examinations of CP in both batch and continuous mode RO processes were carried out. It was demonstrated that the film/KS model gave an adequate description. To quantitatively assess the impact of flow rate on the CP, we derived a Sherwood correlation as a means of predicting the degree of CP and the permeate flux. The herein proposed Sherwood correlation (*Eqs 18, 19 and 20*) was fully validated by the experimental observations, indicating possible applications to SWM ROs with different geometrical properties (e.g. different feed channel heights and lengths). It was found that the newly established Sherwood correlation for batch-RO gave accurate CPF within less than 10% deviation; for continuous RO, the correlation predicted CP more accurately than other popular correlations. The optimum re-circulation rate for DesaLink operation was investigated based on the specific mass transport characterization for

22

batch-RO operation. It may be argued that the optimum feed flow rate determined here may lead to a lower performance for other batch-RO in different scale and using different components, thus limiting its wider applicability. It was, nevertheless, satisfactory in the scope of this work. Furthermore, with the established Sherwood correlation, we were able to evaluate the *CPFs* under the different feed flow rates and to quantify the total volume and concentration of the permeate.

Acknowledgements

23

Figure legends:

Figure 1 Schematic diagram of the solute fluxes across RO membranes

Figure 2 Schematic of practical operation process of batch-RO system (DesaLink): initially both the pump cylinder and RO module are filled with saline water, (1) pressurisation stage (with valve 3 open, valves 1 and 2 closed) the piston pressurises the water, causing freshwater to pass through the membrane. The concentration of solution increases gradually. The concentrations at the inlet and the outlet of the module are kept nearly equal with the help of the re-circulation pump. After the pump piston reaches the end of the cylinder, only concentrated brine is left in the module. Thus, it is necessary to purge the module by introducing feed water (with valves 1 and 2 open, valve 3 closed). In the purging stage (2), the concentration at the outlet decreases towards the value at the inlet. After washing out the left concentrate, the feed pump feeds saline water into the cylinder to move the piston upwards (with valves 1 and 3 open while valve 2 is closed); thus, the whole system is refilled (3) and restored to its ready-to-go state. The water flow paths and no-flow paths of all the pipes are shown by bold and dashed lines respectively [8] .

Figure 3 Schematic diagram (a) and experimental set-up (b) for the mass transport experiments, using the mechanically powered batch-RO system; for details refer to [8, 34].

Figure 4 Experimental set-up for the mass transport experiment, using conventional RO process, i.e. continuous RO operation.

Figure 5 Observed solute removal (R_o) by membrane elements with respect to permeate flux (J_v): (a) XLE-2540 element (with the zoom-in figure shown in (c)), (b) BW30-2540 element (with the zoom-in figure shown in (d)), in continuous RO operation.

Figure 6 The average concentration of permeate (C_{p_ave}) using feed water with different concentrations with respect to initial feed pressure ($P_{power\_initial}$): (a) XLE-2540 membrane element, (b) BW30-2540 membrane element, in un-steady operation

24

Figure 7 Instantaneous feed flow rates measured during the pressurization process of batch-RO. For each experimental set there were two obvious stages of power feeding: first with compressed air feed on, and then switch off at the minimum point of the curve, at about t=180s, after which the flow increases slightly. For more details refer to [34]. Different feed flow rate Q_f were realized by adjusting the re-circulation pump rate from large (2.4 l·min^{-1}), medium (2.0 l·min^{-1}) and small (1.6 l·min^{-1}), the feed concentration being kept the same.

Figure 8 Permeate flow rate profiles for the two different feed flow rates (they are coloured according to Figure 7). Similar to the above observed changing of feed flow, all the permeate flows display a two-stage feature.

Figure 9 Concentration profiles for the permeate flows obtained at the different feed flow rates

Figure 10 Representative increasing concentration of bulk solution in batch-RO process

Figure 11 Comparison of the experimental with the predicted values based on the developed Sherwood correlation (Eq. 18)

Figure 12 Variation of the mass transfer coefficient as a function of the feed flow velocity for the two cases of large and small feed flow rates in batch-RO process

Figure 13 CP value obtained at the different feed flow rates

Figure 14 Calculated CP vales as a function of crossflow velocity (u): (a) XLE-2540 membrane element, (b) BW30-2540 membrane element, under steady RO operation

Figure 15 Effect of crossflow velocity (u) on mass transfer coefficient (k): (a) XLE-2540 membrane element, (b) BW30-2540 membrane element, under steady RO operation

Figure 16 Experimental and fitted Sherwood numbers (Sh) with respect to Reynolds number (Re) at various crossflow velocities: (a) XLE-2540 membrane element, (b) BW30-2540 membrane element, under steady RO operation
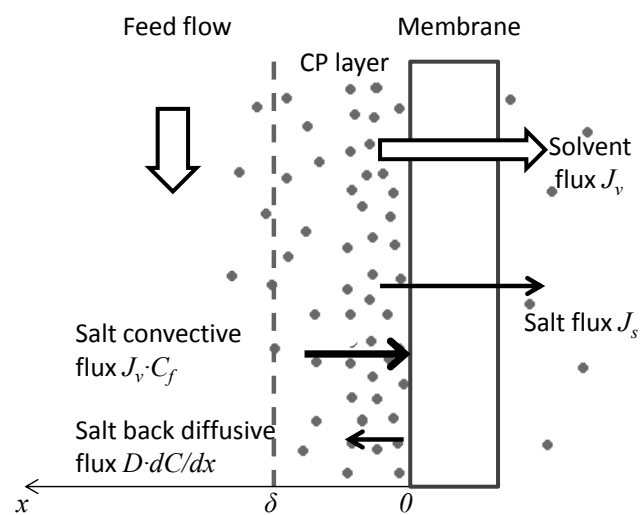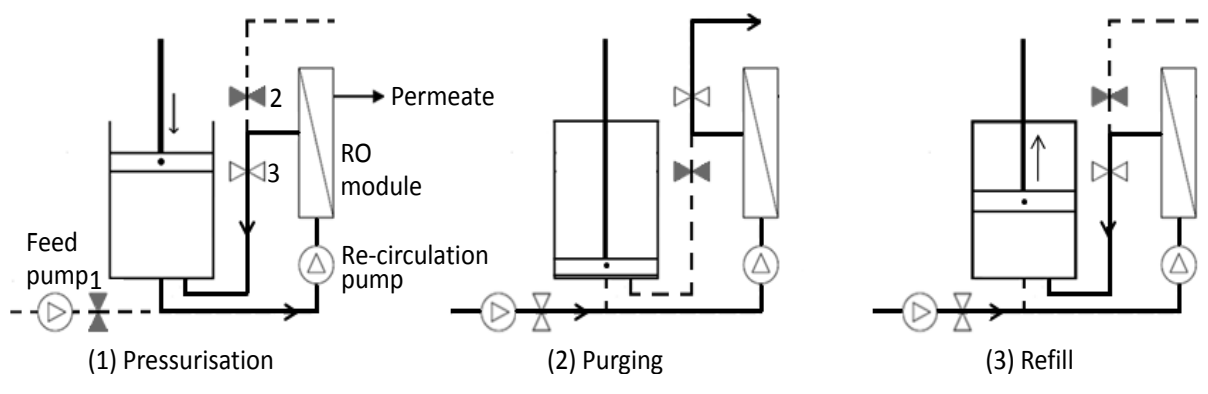
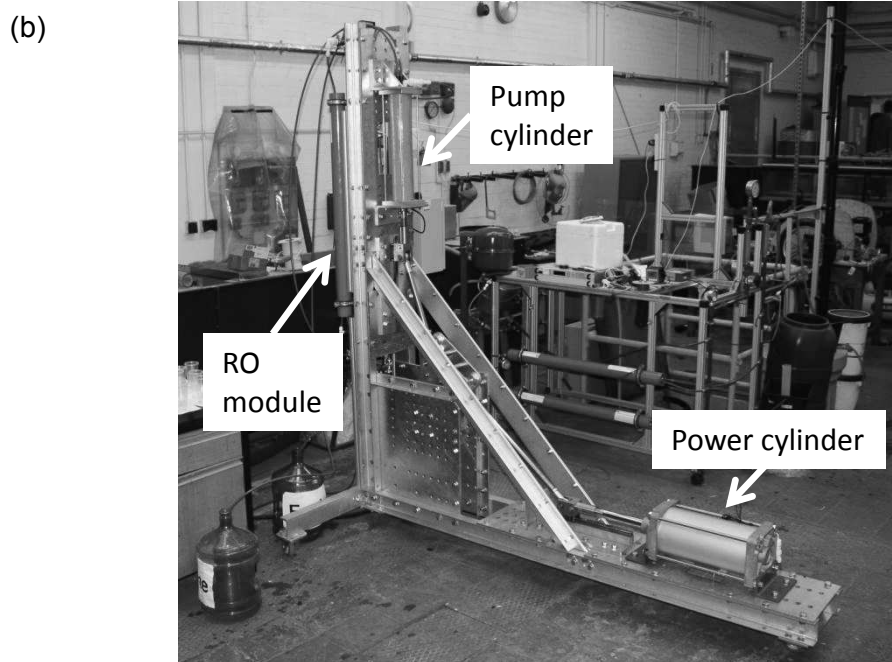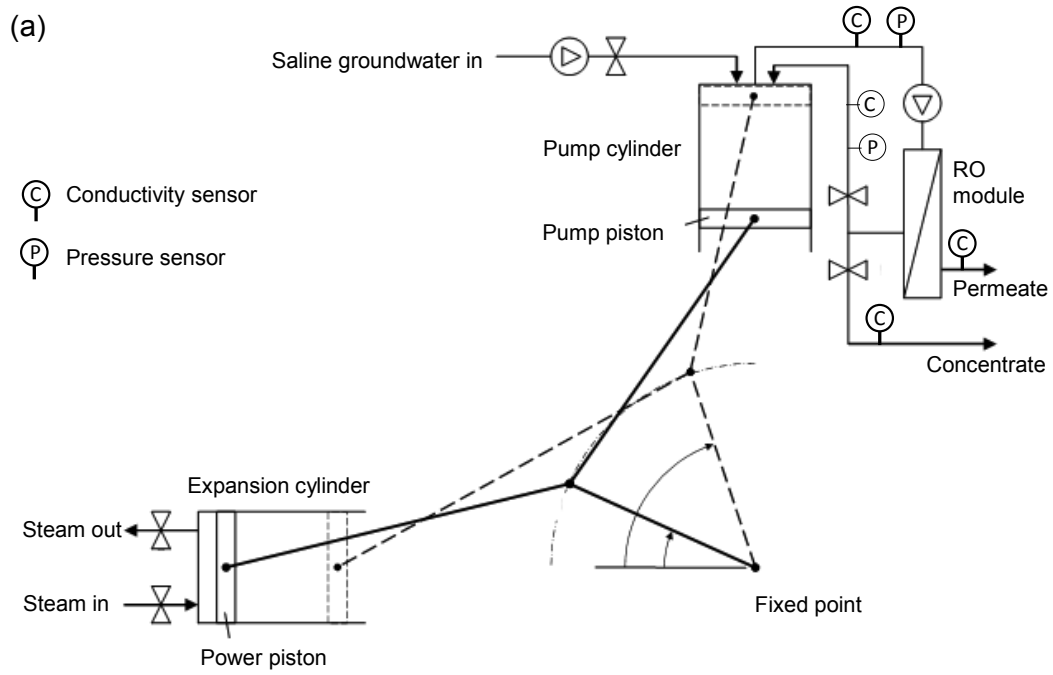*Figure 17 Energy consumptions against different feed flow rates*

References

1. Smalley, R.E., *Future global energy prosperity: the terawatt challenge.* MRS Bulletin, 2005. **30**(06): p. 412-417.
2. Li, C., Y. Goswami, and E. Stefanakos, *Solar assisted sea water desalination: A review.* Renewable and Sustainable Energy Reviews, 2013. **19**: p. 136-163.
3. Ghermandi, A. and R. Messalem, *Solar-driven desalination with reverse osmosis: the state of the art.* Desalination and water treatment, 2009. **7**(1-3): p. 285-296.
4. Qiu, T. and P. Davies, *The scope to improve the efficiency of solar-powered reverse osmosis.* Desalination and Water treatment, 2011. **35**(1-3): p. 14-32.
5. Pérez-González, A., et al., *State of the art and review on the treatment technologies of water reverse osmosis concentrates.* Water Research, 2012. **46**(2): p. 267-283.
6. Manolakos, D., et al., *Identification of behaviour and evaluation of performance of small scale, low-temperature Organic Rankine Cycle system coupled with a RO desalination unit.* Energy, 2009. **34**(6): p. 767-774.
7. Li, C., et al., *Performance investigation of concentrating solar collectors coupled with a transcritical organic Rankine cycle for power and seawater desalination co-generation.* Desalination, 2013. **318**: p. 107-117.
8. Davies, P.A., *A solar-powered reverse osmosis system for high recovery of freshwater from saline groundwater.* Desalination, 2011. **271**(1–3): p. 72-79.
9. Qiu, T., O. Igobo, and P. Davies, *DesaLink: solar powered desalination of brackish groundwater giving high output and high recovery.* Desalination and Water treatment, 2013. **51**(4-6): p. 1279-1289.
10. Qiu, T. and P.A. Davies, *Longitudinal dispersion in spiral wound RO modules and its effect on the performance of batch mode RO operations.* Desalination, 2012. **288**: p. 1-7.
11. Sablani, S., et al., *Concentration polarization in ultrafiltration and reverse osmosis: a critical review.* Desalination, 2001. **141**(3): p. 269-289.
12. Malaeb, L. and G.M. Ayoub, *Reverse osmosis technology for water treatment: state of the art review.* Desalination, 2011. **267**(1): p. 1-8.
13. Lee, S., G. Amy, and J. Cho, *Applicability of Sherwood correlations for natural organic matter (NOM) transport in nanofiltration (NF) membranes.* Journal of Membrane science, 2004. **240**(1): p. 49-65.
14. Gilron, J., N. Gara, and O. Kedem, *Experimental analysis of negative salt rejection in nanofiltration membranes.* Journal of Membrane Science, 2001. **185**(2): p. 223-236.
15. Bhanushali, D., S. Kloos, and D. Bhattacharyya, *Solute transport in solvent-resistant nanofiltration membranes for non-aqueous systems: experimental results and the role of solute–solvent coupling.* Journal of Membrane Science, 2002. **208**(1): p. 343-359.
16. Chaudry, M.A., *Water and ions transport mechanism in hyperfiltration with symmetric cellulose acetate membranes.* Journal of Membrane science, 2002. **206**(1): p. 319-332.
17. Ghiu, S.M.S., *Mass transfer of ionic species in direct and reverse osmosis processes.* 2003, University of South Florida.
18. Mochizuki, S. and A.L. Zydney, *Dextran transport through asymmetric ultrafiltration membranes: comparison with hydrodynamic models.* Journal of Membrane Science, 1992. **68**(1): p. 21-41.
19. Tandon, A., S.K. Gupta, and G.P. Agarwal, *Modelling of protein transmission through ultrafiltration membranes.* Journal of Membrane science, 1994. **97**: p. 83-90.
20. Brian, P.L.T., *Concentration Polar zation in Reverse Osmosis Desalination with Variable Flux and Incomplete Salt Rejection.* Industrial & Engineering Chemistry Fundamentals, 1965. **4**(4): p. 439-445.
21. Jonsson, G. and C. Boesen, *Concentration polarization in a reverse osmosis test cell.* Desalination, 1977. **21**(1): p. 1-10.

27

22. Sutzkover, I., D. Hasson, and R. Semiat, *Simple technique for measuring the concentration polarization level in a reverse osmosis system.* Desalination, 2000. **131**(1): p. 117-127.

23. Efraty, A., *Closed circuit desalination series no-4: High recovery low energy desalination of brackish water by a new single stage method without any loss of brine energy.* Desalination and Water Treatment, 2012. **42**(1-3): p. 262-268.

24. Efraty, A. and J. Septon, *Closed circuit desalination series no-5: high recovery, reduced fouling and low energy nitrate decontamination by a cost-effective BWRO-CCD method.* Desalination and Water Treatment, 2012. **49**(1-3): p. 384-389.

25. Qiu, T.Y. and P.A. Davies, *Comparison of Configurations for High-Recovery Inland Desalination Systems.* Water, 2012. **4**(3): p. 690-706.

26. Ho, W.W. and K.K. Sirkar, *Membrane handbook.* 1992: Springer.

27. Gekas, V. and B. Hallström, *Mass transfer in the membrane concentration polarization layer under turbulent cross flow: I. Critical literature review and adaptation of existing sherwood correlations to membrane operations.* Journal of Membrane Science, 1987. **30**(2): p. 153-170.

28. Bird, R.B., W.E. Stewart, and E.N. Lightfoot, *Transport phenomena.* 2007: John Wiley & Sons.

29. Xuesong, W., *Mass transfer and the fluidized bed intensification of reverse osmosis.* Desalination, 1987. **62**: p. 211-220.

30. Cussler, E.L., *Diffusion: mass transfer in fluid systems.* 2009: Cambridge university press.

31. Schwinge, J., et al., *Spiral wound modules and spacers: review and analysis.* Journal of Membrane Science, 2004. **242**(1): p. 129-153.

32. Spiegler, K. and O. Kedem, *Thermodynamics of hyperfiltration (reverse osmosis): criteria for efficient membranes.* Desalination, 1966. **1**(4): p. 311-326.

33. Goldberg, D.E., *Genetic algorithms in search, optimisation and machine learning.* 1989: Addison-Wesley.

34. Qiu, T.Y., *Desalination of Brackish Water by a Batch Reverse Osmosis DesaLink System for use with Solar Thermal Energy (PhD thesis).* 2013, Aston University.

Figures1-doc

Feed flow　　　　　Membrane

CP layer

Solvent
flux J_v

Salt flux J_s

Salt convective
flux $J_v \cdot C_f$

Salt back diffusive
flux $D \cdot dC/dx$

x　　　　　δ　　　0

Figures2

(1) Pressurisation

Feed pump 1

2

3

RO module

Permeate

Re-circulation pump

(2) Purging

(3) Refill

(a)

Saline groundwater in

© Conductivity sensor

℗ Pressure sensor

Pump cylinder

Pump piston

Expansion cylinder

Steam out

Steam in

Power piston

RO module

Permeate

Concentrate

Fixed point

(b)

Pump cylinder

RO module

Power cylinder

Pulsation Dampener

RO module

Cartridge filters

Conductivity Transmitter

Mixing Bucket

Conductivity Probe

Feed Pump

Feed Tank

Figure 5 - revised

(a)

(b)

(c)

(d)

Figures6-doc

(a)

(b)

Figures11-doc

(a)

(b)

Figure15-doc

(a)

(b)

Figures17-doc